



## Simulation of Doubly Fed Induction generator (DFIG) for Steady state analysis when connected to a wind farm for power system stability

Njeh Edwin Mbabit <sup>a,\*</sup>, David Afungchui<sup>a</sup>, Joseph Ebobenow<sup>b</sup>, Ali Helali<sup>c</sup>, Charles Tabod<sup>a</sup>

<sup>a</sup> Department of Physics, Faculty of Science, The University of Bamenda, PO Box, 39 Bambili. NWR, Cameroon.

<sup>b</sup> Department of Physics, Faculty of Science, University of Buea, PO Box, 63 Buea. SWR, Cameroon.

<sup>c</sup> Mechanical Laboratory, Higher Institute of Transport and Logistics, National Engineering School of Sousse, University of Sousse, P.O. Box 4023, Riadh City, Sousse-Tunisia.

### ARTICLE INFO

#### Article history:

Received March 5, 2024

Accepted December 18, 2024

#### Keywords:

DFIG's,  
Wind Turbine,  
MPPT,  
Swing equation,  
Wind farm,  
Power system stability.

### ABSTRACT

In this paper, a 2MW variable speed, pitch-regulated Doubly-fed Induction Generator (DFIG) with a speed range of 800-2000 rpm was studied for steady-state analysis. The DFIG was modelled in the Matlab/Simulink environment. The rotor-side converter utilized closed-loop stator flux-oriented vector control for managing the DFIG model. This method allows for rapid control and experimenting of grid-connected, variable speed DFIG wind turbines to examine their steady-state and energetic characteristics beneath ordinary and disturbed wind conditions when connected to a wind farm. The steady-state behavior of the wind turbine generator was derived at two different magnetizing levels: one with the reactive power of the stator equal to zero ( $Q_s = 0$ ), and the other with the direct current of the rotor equal to zero ( $I_{dr} = 0$ ). Simulation results show that the machine has higher efficiency when magnetized through the stator as compared with magnetization of the machine through the rotor. To come out with the DFIG transitory stability simulation results traditional controllers' for active and reactive power were compared with an adaptive tracking, self-tuned feedforward proportional integral regulating model for peak performance. Additionally, stability and instability were studied by solving the Swing equation using the Runge-Kutta method of order four. In a steady-state condition for the generator, the acceleration torque ( $T_a$ ) reaches zero, which signifies that the mechanical torque ( $T_m$ ) matches the electrical torque ( $T_e$ ). In the stability investigation,  $T_m$  is assumed to be constant. The findings provide valuable insights into the control strategies required for enhancing the reliability and efficiency of wind turbines in variable wind conditions.

\* Corresponding author, Email address: [mbabitnjah@yahoo.com](mailto:mbabitnjah@yahoo.com)

Tel: +237651322670



## **1. INTRODUCTION**

With the world's increasing population, there is a rising need for electrical energy and a rapid depletion of non-renewable energy sources. This situation has created an urgent need for alternative clean and sustainable energy sources, such as wind energy. In recent years, wind power has emerged as one of the most critical and promising sources of renewable energy. It requires additional transmission capacity and improved methods for maintaining system reliability. Consequently, scientists are increasingly focusing on generating electricity using renewable energy resources.

This study is derived by the benefits of wind turbines (WT) generators employing a Doubly Fed Induction Generator (DFIG), comprising maximum power point tracking (MPPT), variable speed constant frequency (VSCF) operation, management strategies for active and reactive power regulation, as well as voltage control at the point of common coupling (PCC). The wind energy conversion chain can be divided into two categories: vertical-axis wind generators and horizontal-axis wind generators (Andersson et al., 2021). The latter is often preferred due to its advantages (Njiri & Söffker, 2016; Shourangiz-Haghighi et al., 2020). The horizontal-axis wind turbine structure consists of mechanical elements (blades, shaft, gearbox) and electrical elements (DFIG, power cable, power electronic interface, transformer). These devices are designed to transform kinetic energy into electrical energy to supply the grid (Karimirad, 2014; Mastoi et al., 2022). Wind-powered systems based on doubly-fed generators are the most common due to their many benefits, including operation over a wide speed range (Zhou et al., 2023). The operation of variable-speed wind turbines offers several benefits compared to fixed-speed models, including enhanced energy capture, the ability to operate at the maximum power point, greater efficiency, and superior power quality (Müller et al., 2002). Additionally variable-speed WT is the most popular for extracting maximum energy from the wind (Artigao et al., 2018). However, Conventional variable-speed WT generators do not regulate frequency, causing variations in the grid frequency, which underscores the need for frequency control technologies in WT generators (Artigao et al., 2018; Dao et al., 2019; Li & Li, 2021).

The Doubly Fed Induction Generator (DFIG) is esteemed in the context of wind turbine (WT) generators. In a DFIG setup, the stator windings are directly linked to the grid, while the rotor windings connect through slip rings and utilize back-to-back voltage source converters. (Justo et al., 2015). The DFIG features two voltage sources; one from the stator and another from the rotor, and its control is more complex than that of other machines due to the ability to operate at range sub-synchronous and super-synchronous speeds (Kaloi et al., 2016). The DFIG configuration presents several challenges for the power generation system, and to meet these challenges. To address these challenges, scientists have developed various algorithms for controlling and monitoring these systems (Tanvir et al., 2015). These include steady-state analysis, known for its thorough examination, which provides us with data on all system parameters (Gianto, 2021).

In the study by Boukili et al. (2020), an open-circuit stator negative sequence rotor current control enables the generated stator voltage to align with the grid system's voltage imbalance, which promotes an efficient connection of the DFIG to the grid. Moreover, particle swarm optimization and support vector regression were used to estimate wind speed to improve MPPT control (Eltamaly et al., 2020).

In wind energy conversion systems, various algorithms are utilized, with MPPT algorithm being one of the most famous. MPPT algorithms are extensively utilized in systems for converting renewable energy, such as photovoltaic (PV) systems and wind energy conversion systems (WECS).

The primary purpose of the MPPT algorithm is to elicit the maximum power from WECS. The two fundamental MPPT algorithms are direct power control (DPC) and indirect power control (IPC). The IPC method pre-estimates the generated power using wind speed graphs, whereas the DPC method

directly measures electrical power to ensure the wind turbine generator works at maximum power (Mousa *et al.*, 2021; Pande *et al.*, 2021).

Numerous attempts have been undertaken to conduct steady-state analysis (SSA) of the DFIG reflecting its growing influence. A detailed SSA, combined with a computer simulation models and performance analysis, provides a thorough insight into the operational characteristics of DFIG wind turbines.

In 2018, a steady-state mathematical model of the DFIG was determined by employing the spatial vector method for different facilitates the determination of operating areas of the wind turbine generator (Contreras Quispe *et al.*, 2018). This technique operating points based on data and parameters of the wind turbine generator. In 2018, (Nora *et al.*, 2018) implemented stator flux-oriented vector control for DFIG-based wind turbines generators, utilizing space vector pulse width modulation demonstrating its enhanced performance. Similarly, in 2019, Nam *et al.* performed computer simulations of DFIG and implemented vector control for the grid-side converter (GSC) as well as rotor-side converter (RSC) to deliver active power to the grid.

Following that, the topic of stator field-oriented control (SFOC) for the doubly-fed induction generator (DFIG) was addressed. (Zerzeri *et al.*, 2019), depending on the sliding mode flux observer algorithm, the scheme was found to be efficient under parameter variations. In 2020, (I. *et al.*, 2020) presented steady-state analysis (SSA) of the DFIG alongside various magnetizing strategies tailored for specific wind turbine operating modes. Their mathematical modeling approach utilizing stator flux-oriented vector control was found effective, utilizing stator terminal quantities (I. *et al.*, 2020). The mathematical modeling of DFIG in SSA adopting stator flux-oriented vector control was discovered to be effectual as it uses the quantity of stator terminal. Finally, in 2021, Sharawy *et al.* discussed a simplified SS modeling of DFIG and its operational characteristics in an independent wind energy conversion system with rotor control (Sharawy *et al.*, 2021)

An SSA strategy was later proposed for the synchronous Doubly-Fed Induction Generator (DFIG), focusing on stator voltage references for the Grid Side Converter (GSC) and rotor flux references for the Rotor Side Converter (RSC). The analysis concluded that the synchronous DFIGs performs effectively when the speed of the wind are below their critical values (Li & Li, 2021). In a separate study by Arjun *et al.* (2021), a discussion centered on DFIG rotor flux orientation vector control emphasizing machine modeling suitable for a wide range of operating speed.

Karthik *et al.* (2022) introduced a method to compute steady-state (SS) values of DFIG using a precise procedure. Results of the simulation in the time-domain indicated that the SS values align with the initialization values. Building upon this research, the integration of steady-state analysis with a functional computer simulation model appears promising.

The importance of the paper lies in establishing that, for the DFIG, a unique solution exists for the rotor control variables—rotor voltage ( $V_r$ ) and rotor flux ( $\Psi$ )—exists for every SS operating point. This finding facilitates the derivation of SS aspect from a given torque-speed pattern for a three-bladed wind turbine, thereby ensuring stability and preventing numerical instability. Additionally, the paper contributes significantly by presenting parameter-dependent steady-state investigation of the DFIG within a variable speed wind energy conversion structure. The study's focus on magnetizing the DFIG through both the rotor and stator enhances understanding of its steady-state performance. The simulation was employed to examine the DFIG over a broad speed interval from 800 to 2000 rpm. The SSA under various operating modes provided understanding into the system's behaviour, including variations in stator, rotor active power, current, and voltage.

## **2. DESCRIPTION OF INDUCTION GENERATOR**

The induction machine can be represented by six coils. With three in the stator as well as in the rotor which are labelled respectively as;  $a_1$ ,  $b_1$ ,  $c_1$  and  $a_2$ ,  $b_2$ ,  $c_2$ . The axis of coil  $a_2$  is utilized as the reference

frame, which is stationary. The rotor rotates at a speed of  $\omega_2$ , with angle  $\theta_2$  between the reference and rotor frames. The six windings result in 36 inductances, representing all possible combinations.

The relationship between voltages and currents provides the basis for deriving the flux linkage  $\lambda$  in this induction machine, as shown in the subsequent expression:

$$\lambda = \ell i \tag{1}$$

The voltage is defined as the rate of change of the flux linkage

$$v = \frac{d}{dt} \lambda = \frac{d}{dt} \ell i = \ell \frac{d}{dt} i + \left( \frac{d}{dt} \ell \right) i \tag{2}$$

Here, the wedding voltage is represented by the vector  $v$ , while the winding currents are indicated by the vector  $i$ , and  $\ell$  stands for the inductance. Assuming a balanced system and adopting a rotating reference frame instead of the stator's stationary reference frame, the induction machine connects to a balanced three-phase system. In a balanced system, the phasor sum of all three currents is zero.

$$i_{a1} + i_{b1} + i_{c1} = 0 \tag{3}$$

Using the relationship in Eq. (3), we can simplify Eq. (2); For instance, consider the flux linkage of phase a:

$$\lambda_{a1} = L_{s1}i_{a1} + L_{m1}i_{b1} + L_{m1}i_{c1} + \ell_{14}i_{a2} + \ell_{15}i_{b2} + \ell_{16}i_{c2} \tag{4}$$

$$\lambda_{a1} = L_{11}i_{a1} + \ell_{14}i_{a2} + \ell_{15}i_{b2} + \ell_{16}i_{c2} \tag{5}$$

This process is repeated for all three phases. The model of the machine was developed by Robert Park based on the theory of rotating frame. The objective is to find a relationship between voltage and currents of all windings. The voltage is a flux linkage change rate, that is,

$$v_{abc} = \frac{d}{dt} \lambda_{abc} = \frac{d}{dt} (B^{-1} \lambda_{dqo}) = \left( \frac{d}{dt} B^{-1} \right) \lambda_{dqo} + B^{-1} \left( \frac{d}{dt} \lambda_{dqo} \right) \tag{6}$$

Because,

$$v_{abc} = B^{-1} v_{dqo} \tag{7}$$

Hence

$$v_{dqo} = B \left( \frac{d}{dt} B^{-1} \right) \lambda_{dqo} + \left( \frac{d}{dt} \lambda_{dqo} \right) \tag{8}$$

Utilizing the general matrix equation framework, we can define the voltage in the direct-quadrature (d-q) frames as an equation that incorporates both the stator and rotor voltages.

$$\begin{bmatrix} v_{dqo1} \\ v_{dqo2} \end{bmatrix} = \begin{bmatrix} B_1 & 0 \\ 0 & B_2 \end{bmatrix} \begin{bmatrix} v_{abc1} \\ v_{abc2} \end{bmatrix} \tag{9}$$

Where; 
$$B = \begin{bmatrix} B_1 & 0 \\ 0 & B_2 \end{bmatrix} \tag{10}$$

The current and flux linkage can be addressed in the same way. The relationships are given as;

$$\begin{cases} i_{dqo} = Bi_{abc} \\ \lambda_{dqo} = B\lambda_{abc} \end{cases} \quad (11)$$

The above analysis in the rotating frame is to simplify the inductance matrix and make it time invariant. This can be done by further processing Eq. (11)

$$\lambda_{dqo} = B\lambda_{abc} = B\ell_{abc}i_{abc} = B\ell_{abc}B^{-1}i_{dqo} = \ell_{dqo}i_{dqo} \quad (12)$$

$$\ell_{dqo} = B\ell_{abc}B^{-1} = \begin{bmatrix} L_{11} & 0 & 0 & L_{12} & 0 & 0 \\ 0 & L_{11} & 0 & 0 & L_{12} & 0 \\ 0 & 0 & L_{11} & 0 & 0 & 0 \\ L_{12} & 0 & 0 & L_{22} & 0 & 0 \\ 0 & L_{12} & 0 & 0 & L_{22} & 0 \\ 0 & 0 & 0 & 0 & 0 & L_{22} \end{bmatrix} \quad (13)$$

Substituting B in Eq. (10) into Eq. (8) and removing the zero sequence components gives Eq. (14)

$$\begin{bmatrix} v_{d1} \\ v_{q1} \\ v_{d2} \\ v_{q2} \end{bmatrix} = \begin{bmatrix} 0 & -\omega & 0 & 0 \\ \omega & 0 & 0 & 0 \\ 0 & 0 & 0 & -s\omega \\ 0 & 0 & s\omega & 0 \end{bmatrix} \begin{bmatrix} \lambda_{d1} \\ \lambda_{q1} \\ \lambda_{d2} \\ \lambda_{q2} \end{bmatrix} + \frac{d}{dt} \begin{bmatrix} \lambda_{d1} \\ \lambda_{q1} \\ \lambda_{d2} \\ \lambda_{q2} \end{bmatrix} \quad (14)$$

Where  $\omega = 2\pi f$ , f represents the frequency of the supply voltage. By utilizing the speed voltage and transformer voltage, the steady-state model of the induction machine was analysed to understand its performance characteristics under different operating conditions

### 2.1 Steady-State Model

The first term in Eq. (14) is called “speed voltage,” and the second term is called “transformer voltage.” For balanced system, the transformer voltage is zero as,

$$\frac{d}{dt} \begin{bmatrix} \lambda_{d1} \\ \lambda_{q1} \\ \lambda_{o1} \\ \lambda_{d2} \\ \lambda_{q2} \\ \lambda_{o2} \end{bmatrix} = \frac{d}{dt} B \begin{bmatrix} \lambda_{a1} \\ \lambda_{b1} \\ \lambda_{c1} \\ \lambda_{a2} \\ \lambda_{b2} \\ \lambda_{c2} \end{bmatrix} = \frac{d}{dt} B \begin{bmatrix} \lambda_{max1} \cos(\omega t) \\ \lambda_{max1} \cos(\omega t - 120) \\ \lambda_{max1} \cos(\omega t + 120) \\ \vdots \\ \vdots \\ \vdots \end{bmatrix} = \frac{d}{dt} \begin{bmatrix} \lambda_{max1} \\ 0 \\ 0 \\ \vdots \\ \vdots \\ \vdots \end{bmatrix} = \begin{bmatrix} 0 \\ 0 \\ 0 \\ \vdots \\ \vdots \\ \vdots \end{bmatrix} \quad (15)$$

Hence

$$\begin{bmatrix} v_{d1} \\ v_{q1} \\ v_{d2} \\ v_{q2} \end{bmatrix} = \begin{bmatrix} 0 & -\omega & 0 & 0 \\ \omega & 0 & 0 & 0 \\ 0 & 0 & 0 & -s\omega \\ 0 & 0 & s\omega & 0 \end{bmatrix} \begin{bmatrix} \lambda_{d1} \\ \lambda_{q1} \\ \lambda_{d2} \\ \lambda_{q2} \end{bmatrix} \quad (16)$$

Substituting  $\lambda$  in Eqs. (12) and (13) into Eq. (16) yields

$$\begin{bmatrix} v_{d1} \\ v_{q1} \\ v_{d2} \\ v_{q2} \end{bmatrix} = \begin{bmatrix} 0 & -\omega L_{11} & 0 & -\omega L_{12} \\ \omega L_{11} & 0 & \omega L_{12} & 0 \\ 0 & -s\omega L_{12} & 0 & -s\omega L_{22} \\ s\omega L_{12} & 0 & s\omega L_{22} & 0 \end{bmatrix} \begin{bmatrix} i_{d1} \\ i_{q1} \\ i_{d2} \\ i_{q2} \end{bmatrix} \quad (17)$$

The winding resistance can now be added to Eq. (17)

$$\begin{bmatrix} v_{d1} \\ v_{q1} \\ v_{d2} \\ v_{q2} \end{bmatrix} = \begin{bmatrix} r_1 & 0 & 0 & 0 \\ 0 & r_1 & 0 & 0 \\ 0 & 0 & r_2 & 0 \\ 0 & 0 & 0 & r_2 \end{bmatrix} \begin{bmatrix} i_{d1} \\ i_{q1} \\ i_{d2} \\ i_{q2} \end{bmatrix} + \begin{bmatrix} 0 & -\omega L_{11} & 0 & -\omega L_{12} \\ \omega L_{11} & 0 & \omega L_{12} & 0 \\ 0 & -s\omega L_{12} & 0 & -s\omega L_{22} \\ s\omega L_{12} & 0 & s\omega L_{22} & 0 \end{bmatrix} \begin{bmatrix} i_{d1} \\ i_{q1} \\ i_{d2} \\ i_{q2} \end{bmatrix} \quad (18)$$

In this scenario,  $r_1$  and  $r_2$  denote the resistances of the stator and rotor windings, respectively. The variable  $S$  signifies the per-unit representation of the speed difference.  $L_{11}$  represents the difference between the self-inductance of a stator winding and the mutual inductance between any pair of stator windings. Likewise,  $L_{22}$  indicates the difference between the self-inductance of a rotor winding and the mutual inductance between any two rotor windings. Furthermore,  $L_{12}$  is equivalent to  $3/2$  of the mutual inductance.

For the four windings in the  $d$ - $q$  frames are represented in Eq. (18). This model is now used to compute any variable such as torque or power.

In the context of current transformation, the stator voltage exhibits similarities in both the  $abc$  frame and the  $dqo$  frame.

$$i_{abc1} = B_1^{-1} i_{dqo1} \quad (19)$$

$$\begin{bmatrix} i_{a1} \\ i_{b1} \\ i_{c1} \end{bmatrix} = \begin{bmatrix} \cos \omega t & -\sin \omega t & 1 \\ \cos(\omega t - 120) & -\sin(\omega t - 120) & 1 \\ \cos(\omega t + 120) & -\sin(\omega t + 120) & 1 \end{bmatrix} \begin{bmatrix} i_{d1} \\ i_{q1} \\ i_{o1} \end{bmatrix} \quad (20)$$

Considering the first of these equations and noting that for a balanced system, the zero sequence current  $i_{o1}$  is zero this then leads to,

$$i_{a1} = i_{d1} \cos \omega t - i_{q1} \sin \omega t \quad (21)$$

The root mean square (rms) of these currents ( $I_{d1}$  and  $I_{q1}$ ) are

$$\begin{cases} I_{d1} = \frac{i_{d1}}{\sqrt{2}} \\ I_{q1} = \frac{i_{q1}}{\sqrt{2}} \end{cases} \quad (22)$$

In phasor form, the current in phase  $a_1$  is

$$\bar{I}_{a1} = I_{d1} + jI_{q1} \quad (23)$$

From Eq. (23), the norm of the current in phase  $a_1$  is

$$I_{a1} = \sqrt{(I_{d1})^2 + (I_{q1})^2} \quad (24)$$

Similarly, we can develop a phasor relationship for the voltage as

$$\bar{V}_{a1} = V_{d1} + jV_{q1} \quad (25)$$

The complex (apparent) power of the generator is calculated by multiplying all voltages by their corresponding conjugate current. The use of the conjugate guarantees that the inductor's reactive power is positive, while for the capacitor, it is negative, adhering to the conventions commonly followed in the power industry. (Xu *et al.*, 2011) introduced a mathematical model of a DFIG operating in a distorted grid voltage environment within a positive synchronous reference frame. They offered an in-depth analysis of the electromagnetic torque fluctuations in the DFIG, along with the active and reactive power dynamics of the stator in the context of grid voltage harmonic distortion.

The complex power of phase  $a_1$  in the stator is given as:

$$\bar{S}_{a1} = \bar{V}_{a1} \bar{I}_{a1}^* \quad (26)$$

For the three phases, the stator power is

$$\bar{S}_1 = 3\bar{V}_{a1} \bar{I}_{a1}^* \quad (27)$$

Substituting the voltage and current in Eqs. (23) and (24) into Eq. (27)

$$\bar{S}_1 = 3(V_{d1} + jV_{q1})(I_{d1} - jI_{q1}) \quad (28)$$

The real component of complex power is associated with real power, whereas the imaginary component signifies reactive power.

$$\begin{cases} P_1 = 3(V_{d1}I_{d1} + V_{q1}I_{q1}) \\ Q_1 = 3(V_{q1}I_{d1} - V_{d1}I_{q1}) \end{cases} \quad (29)$$

Similar expressions can be developed for the rotor circuit with real power and reactive power respectively as,

$$\begin{cases} P_2 = 3(V_{d2}I_{d2} + V_{q2}I_{q2}) \\ Q_2 = 3(V_{q2}I_{d2} - V_{d2}I_{q2}) \end{cases} \quad (30)$$

From analyses the equations for the induction machine in the steady-state operation are,

$$\begin{cases} v_{d1} = r_1 i_{1d} - \omega L_{11} i_{q1} - \omega L_{12} i_{q2} \\ v_{q1} = r_1 i_{q1} + \omega L_{11} i_{d1} + \omega L_{12} i_{d2} \end{cases} \quad (31)$$

Where;  $L_{12}$  equals to  $3/2L_m$ ,  $L_m$  represents the maximum mutual inductance when the two windings between  $a_1$  and  $a_2$  are perfectly aligned. The input and the output physical quantities of the three bladed variable speed wind turbine generator (VSWT) based on DFIG that operate at the sub-synchronous mode at wind speed of 8m/s and at the super-synchronous mode at wind speed of 10m/s with the power of 1.5MW are as follows:

The rotor and stator voltages and mechanical torque are expressed as follows are the input physical quantities:

$$T_m = 2H \frac{d\omega_2}{dt} + T_e \quad (32)$$

$$V_{dq01} = B_1 V_{abc1} \quad (33)$$

$$V_{dq02} = B_2 V_{abc2} \quad (34)$$

The output physical quantities include electromagnetic torque, stator currents, rotor currents and the stator's reactive and active power, expressed as follows:

$$T_e = T_m - 2H \frac{d\omega_2}{dt} \quad (35)$$

$$i_{a1} = i_{d1} \cos \omega t + i_{q1} \cos(\omega t - 90) \quad (36)$$

$$i_{a2} = i_{d2} \cos \omega t + i_{q2} \cos(\omega t - 90) \quad (37)$$

$$Q_2 = 3(V_{q1}I_{d1} - V_{d1}I_{q1}) \quad (38)$$

$$P_1 = 3(V_{d1}I_{d1} + V_{q1}I_{q1}) \quad (39)$$

With electrical and mechanical torque, stability and instability of power injected on the grid at steady state operation was studied by solving the swing equation. The swing equation, a second order differential equation, is express as two first-order differential equations:

$$\frac{2H}{\omega_s} \frac{d\omega}{dt} = P_m - P_e \quad (40)$$

$$\frac{d\delta}{dt} = \omega - \omega_s \quad (41)$$

In this context,  $\omega$ ,  $\omega_s$  and  $\delta$  and are expressed in electrical units. Here,  $\omega_s$  is the synchronous speed in rad/s. The maximum power that can be transferred for a particular excitation is given by  $\frac{E_g V_t}{x_d}$  at  $\delta = 90^\circ$

Where  $E_g$  = Generator internal emf,  $V_t$  = Terminal voltage,  $\theta$  = Power angle,  $X_d$  = Direct axis reactance.

Using Runge Kutta method of order four to solve the Swing equation,  $P_m$  is considered a constant,  $P_e = P_o \sin \delta$  where  $P_o = E_g V_t / x_d$  and  $M = 2H / \omega_s$ . Then

$$\frac{d^2 \delta}{dt^2} = \frac{P_m - P_o \sin \delta}{M} \quad (42)$$

$$\frac{d}{dt} \left( \frac{d\delta}{dt} \right) = \frac{P_m - P_o \sin \delta}{M} \quad (43)$$

$$\frac{d\delta}{dt} = \omega \quad (44)$$

$$\frac{d\omega}{dt} = \frac{P_m - P_o \sin \delta}{M} \quad (45)$$

In solving the swing equation with the initial conditions. Using matlab in plotting delta in rad/s against time in second, the system is unstable when  $P_o$  is less than 1 ( $P_o < 1$ ), because of a fault and is stable for  $P_o$  greater than 1 ( $P_o > 1$ ), when the fault is cleared. The graph of stable and unstable is as shown below in Fig (1).

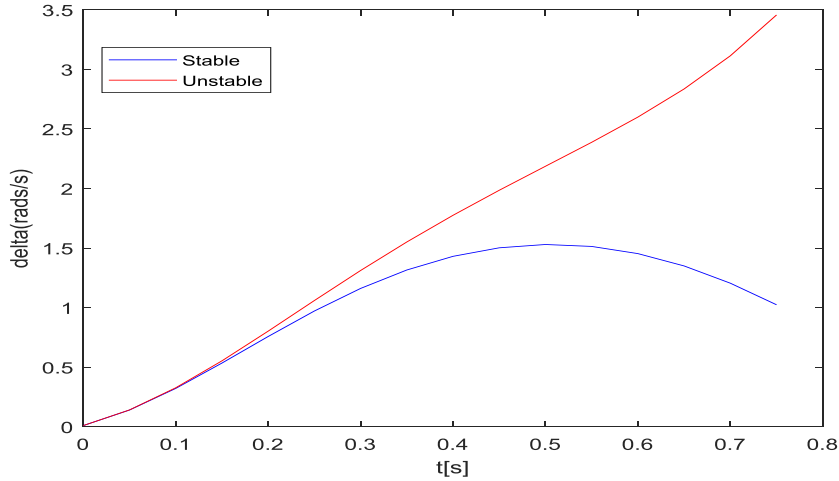


Fig 1. Swing curve ( $\delta$  against  $t$ ) for stable and unstable system.

The power stability and instability on the grid during the steady-state operation of a DFIG linked to a wind farm are significantly impacted by the power extracted from the wind, which is determined by the performance characteristics of the wind turbine.

## 2.2 Characteristics of Wind Turbines

A wind turbine captures the kinetic energy of the wind and converts it into torque to rotate the rotor blades. The relationship between wind energy and the mechanical energy produced by the rotor is influenced by several key factors, such as air density, wind speed, and the rotor's swept area. Wind speed and air density are site-specific climatological parameters.

Power captured from the wind  $P_w$  and converted into electrical converting into electric power, can be computed using methods described in the literature (Arnaltes et al., n.d.; Haque et al., 2010).

$$P_w = \frac{1}{2} \rho C_p A v_\omega^3 \quad (46)$$

According to Equation (46), the air density ( $\rho$ ) is measured in  $\text{kg/m}^3$ , the power coefficient is denoted as  $C_p$ , the area covered by the wind turbine rotor ( $A$ ) is in  $\text{m}^2$ , and the wind speed is represented in  $\text{m/s}$ . The mechanical power ( $P_m$ ) produced by the wind turbine is influenced by the power coefficient ( $C_p$ ) and can be expressed as follows in (Arnaltes et al., n.d.; Chan et al., 2004; Haque *et al.*, 2010; Heier, 2006)

$$P_m = C_p(\lambda, \beta) P_w \quad (47)$$

Here  $\lambda$  is the tip-speed ratio (TSR) and the pitch angle is  $\beta$ . If the pitch angle  $\beta$  is kept unchanged, the relationship between  $C_p$  and  $\lambda$  can be stated as as (Chen & Smedley, 2008; Hansen & Michalke, 2008; Haque *et al.*, 2010)

$$C_p(\lambda) = 0.52 \left( \frac{116}{\lambda - 0.2} - 9 \right) e^{-21/(\lambda - 0.3)} + 0.0068\lambda \quad (48)$$

$C_p$  is often given as function of the tip speed ratio  $\lambda$  which is defined by,

$$C_p = f(\lambda, \beta) \quad (49)$$

Where  $\lambda$  is

$$\lambda = R \left( \frac{\omega_r}{v_w} \right) \quad (50)$$

In this context,  $R$  represents the radius of the wind turbine's aerodynamic rotor measured in meters, while  $\omega_r$  indicates the angular speed of the turbine rotor expressed in rad/s. The mechanical power  $P_m$  generated by the turbine can be maximized by adjusting the turbine's operating point to an optimal value of the power coefficient  $(C_p)_{opt}$ . This optimal value of  $C_p$  can be accomplished by controlling the turbine rotor speed  $\omega_r$ , is controlled to maintain the highest value of  $\lambda$  ( $\lambda_{opt}$ ) as discussed by (Hua Geng et al., 2011; Robinson *et al.*, 2010).

$$(\omega_r)_{opt} = \frac{\lambda_{opt}}{R} v_w \quad (51)$$

Since the wind speed  $v_w$  may change, the speed of rotor has to be adjusted so that  $\lambda_{opt}$  and  $(C_p)_{opt}$  are maintained for capturing the maximum mechanical power  $(P_m)_{max}$  from the wind. The value of  $(P_m)_{max}$  can be determined from

$$(P_w)_{max} = \frac{\rho A}{2} (C_p)_{opt} \left( \frac{(\omega_r)_{opt} R}{\lambda_{opt}} \right)^3 = K_{opt} (\omega_r)_{opt}^3 \quad (52)$$

As a consequence, the optimal torque  $(T_m)_{opt}$  produced by the wind turbine generator can be expressed as (Dahbi et al., 2016; Fortmann, 2015; Karakasis et al., 2019; Keramat Siavash et al., 2020).

$$(T_m)_{opt} = K_{opt} (\omega_r)_{opt}^2 \quad (53)$$

Figure (2) shows  $C_p$  coefficient of wind turbine generator at different pitch angles. According to Equation (53), it is possible to control both the rotor-side and grid-side converters of the DFIG to attain optimal torque.

### 2.3 The DFIG Rotor Side Control

The rotor variables of the DFIG must be aligned in accordance with the defined orientation parameter. Algorithms are implemented, for both stator voltage-oriented control and stator flux-oriented control. After calculating this parameter vector within the rotor orientation framework, the relative angle ( $\delta$ ) to the rotor-side orientation framework is determined, allowing for the conversion of the rotor parameter into the updated control-reference structure.

Vector control is implemented in the rotor-side converter to manage the active and reactive power of the stator. The direct axis loop is tasked with regulating reactive power, whereas the quadrature axis is responsible for controlling active power. The rotor assesses its circuit parameters, monitors the reactive power transfer between the stator and the power grid, and modifies the generator torque accordingly. Although its input parameters are independent of the stator's orientation structure, accurate measurement and control of the stator's target parameters are crucial. To ensure the rotor-side control block (RSC) produces an output compatible with the stator's parameters, the rotor parameters expressed in the rotor's d-q orientation frame must be transformed to align with the control reference frame.

### 2.4 The DFIG Grid side converted control

The grid-side converter in DFIG typically employs a three phase, two-level voltage source converter with insulated-gate bipolar Transistor (IGBT) as a switching device. Its primary function is to regulate

the linkage DC voltage, achieved through a grid voltage-oriented control scheme. In this configuration, the rotating reference frame's dq-axis aligns with the grid voltage.

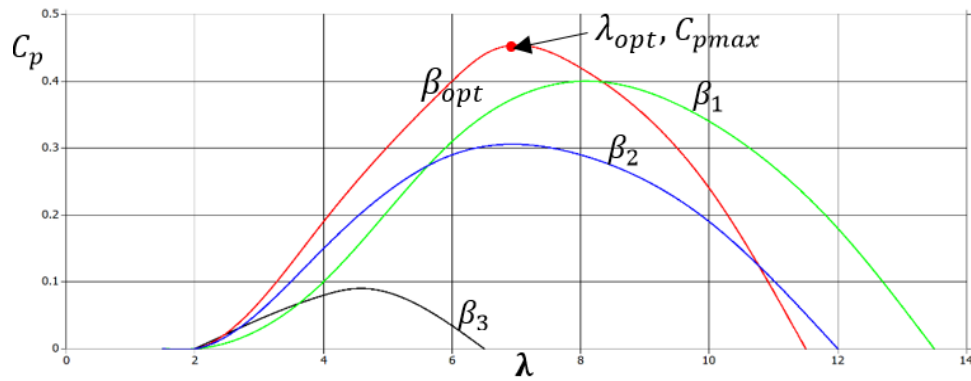


Fig 2. Cp for different pitch angle  $\beta$ , with  $\beta_3 > \beta_2 > \beta_1 > \beta_{opt}$ .

Within the DC link of the grid-side converter, there is a filter capacitor that delivers energy to a load resistance. Its primary goal is to maintain a stable DC link voltage, and optionally, it can provide limited reactive power support. A fundamental assumption in grid converter control is grid stiffness, which implies minimal grid voltage fluctuations. While achieving 100% stiffness is impractical in most cases, any grid voltage fluctuations will affect the linkage DC voltage. Variations in the linkage DC voltage affect the DFIG rotor's reactive power intake through another converter circuit. When the DC link provides sufficient reactive power, the DFIG draws reactive power from the grid to meet its operational needs. The fluctuations in reactive power absorption on the rotor side lead to corresponding adjustments in the stator's reactive power requirements, which in turn causes voltage variations at the point of common coupling

The MPPT of the wind turbine generator is analysed with coordinated control between the rotor-side and grid-side transformers of the DFIG.

### 2.5 Maximum Power Point Tracking of a Wind Turbine Generator

The most commonly utilized wind turbine control approach is shown in Fig (3), which delineates four operational zones. This figure depicts the maximum power and maximum power coefficient as a functions of wind speed, resembling operation at full-load conditions. Mechanical power output in this scenario can be limited by adjusting blade pitch or employing torque control. Typically, the electromagnetic torque is kept at a negligible value, and pitch angle adjustment is utilized to keep the wind turbine generator operating at optimal speed and to sustain higher power output during rated wind speeds.

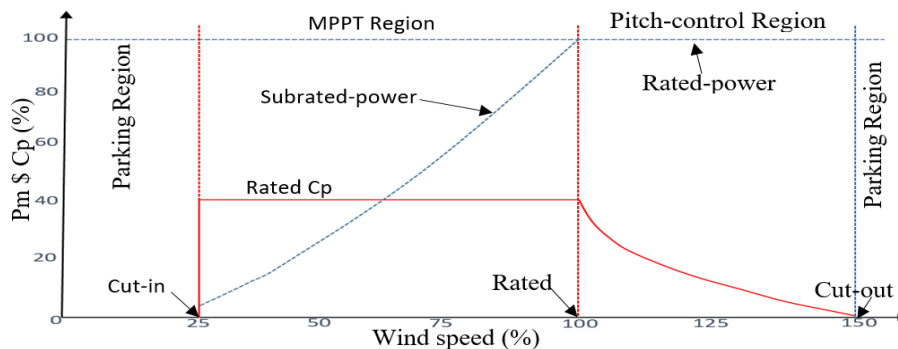


Fig 3. The maximum power point tracking for operation zones of wind turbine generator

To accommodate the irregular nature of wind, it is crucial for the control system to track and maximize peak power output regardless of wind variations. Model Predictive Control (MPC) methods are particularly effective due to their adaptive tracking and self-tuning capabilities. Two primary MPC strategies—direct speed control and indirect speed control—are extensively discussed for their efficacy in wind turbine processes.

### 2.6 Mechanical power against turbine speed for different wind speeds for MPPT

Figure 4 illustrates the mechanical power  $P_m$  generated by the turbine in relation to the rotor speed  $\omega_r$ , with various wind speeds presented in ascending order  $\{6 < 8 < 10 < 12 < 14 < 16\}$  m/s. The figure also includes the curve for  $(P_m)_{max}$ .

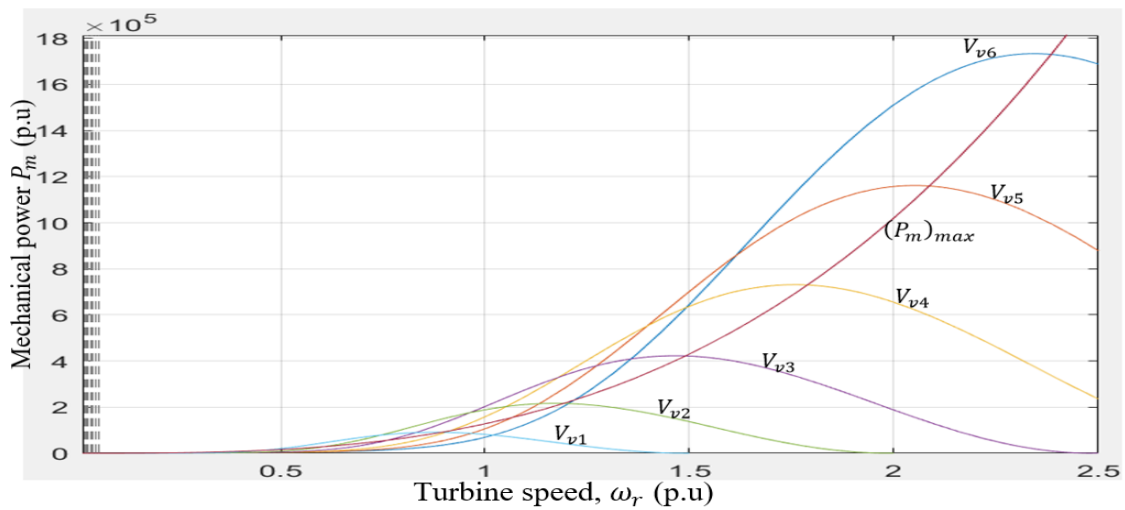


Fig 4. Mechanical power against turbine speed for different wind speeds.

The  $(P_m)_{max}$  curve indicates that for every wind speed, there exist an optimal rotor speed that ensures the maximum power is captured from the wind. This implies that by controlling the generator's speed to maintain the turbine's operation at this optimal point, the turbine can achieve  $(P_m)_{max}$  at any wind speed.

In this part, a simulation for maximum power point tracking of a wind turbine generator was conducted using a 1.5 MW stator power Doubly-Fed Induction Generator (DFIG) model and a three-bladed wind turbine generator model with a gear ratio  $n=100$  and a blade radius of 42 meters, as elaborated in Fig. 3.

### 3. MATLAB SIMULINK MODEL OF A THREE-BLADED WIND TURBINE GENERATOR BASED ON DFIG FOR MPPT

The MATLAB Simulink model of the three-bladed wind turbine generator, based on a Doubly-Fed Induction Generator (DFIG) for maximum power point tracking (MPPT), takes speed and torque arrays as inputs. In the super-synchronous operating mode, the torque is lesser than in the sub-synchronous operating mode. Consequently, due to the increased rotational speed in the super-synchronous mode, the power output is higher than in the sub-synchronous mode. For both modes, as the torque reduces, the rotational speed increases.

The simulation outcomes are presented in Figures 5, 6, 9, and 10. The corresponding variations of the stator current ( $I_s$ ) and rotor current ( $I_r$ ) for the generator operating in the super-synchronous mode at a

rotational speed of 10 m/s and a give power output of 1.5 MW are illustrated in Figures 11 and 12, respectively. Similar results for a rotational speed of 8 m/s are presented in Figures 7 and 8.

At start up, there is significant perturbation because the machine is directly couple to the grid, a scenario that differs from practical applications. This start up transient is disregarded in this analysis, which focuses on the machine’s steady-state conditions.

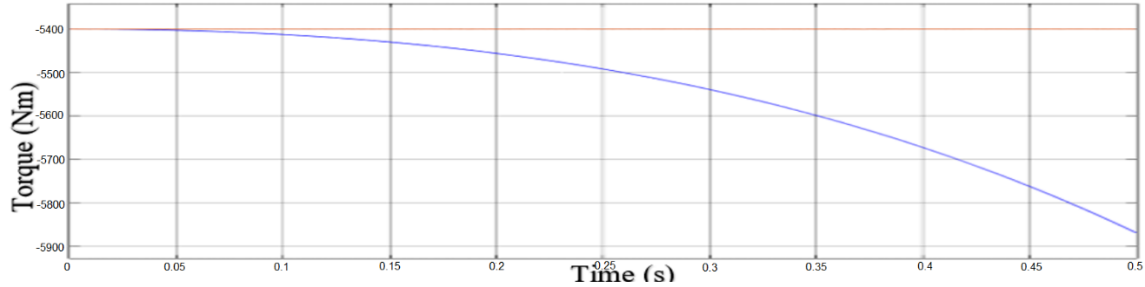


Fig 5. Variation of torque operating at wind speed of 8m/s against time. At this wind speed, the generator is functioning in a sub-synchronous mode.

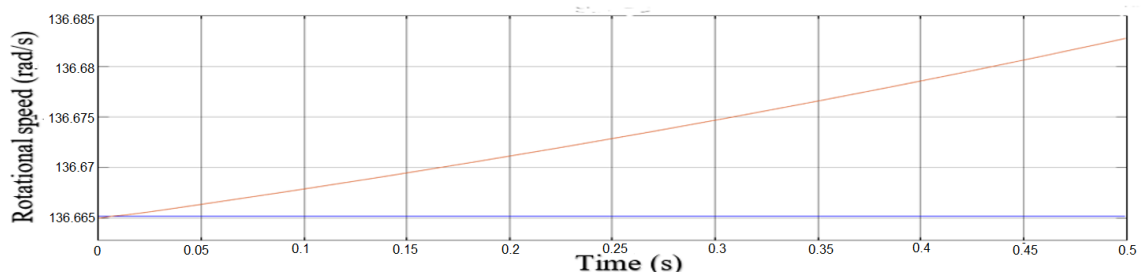


Fig 6. Variation of the rotational speed of 8m/s against time.

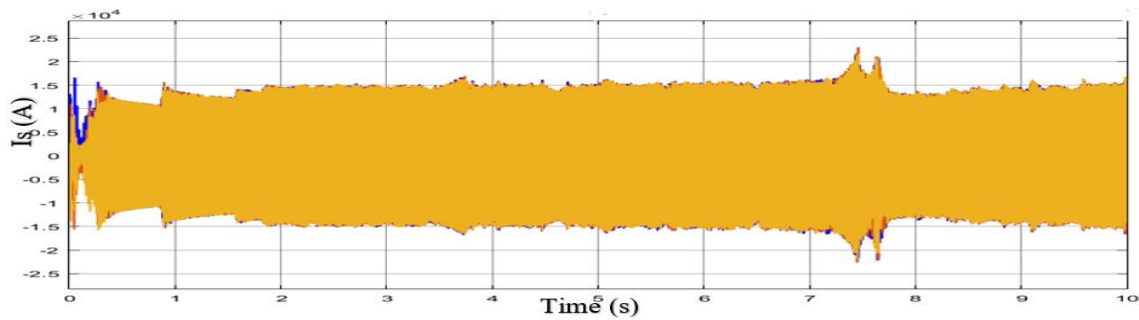


Fig 7. Variation of Is against time when the WT generator is operating at sub-synchronous mode at wind speed of 8m/s.

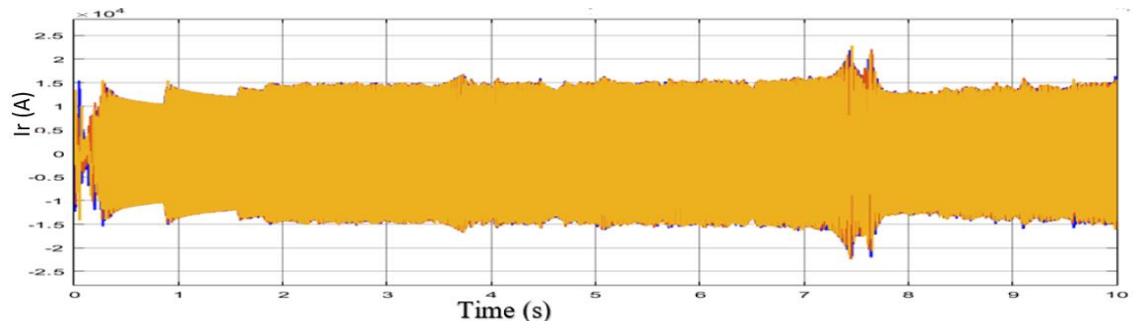


Fig 8. Variation of Ir against time when the WT generator is operating at sub-synchronous mode at wind speed of 8m/s.

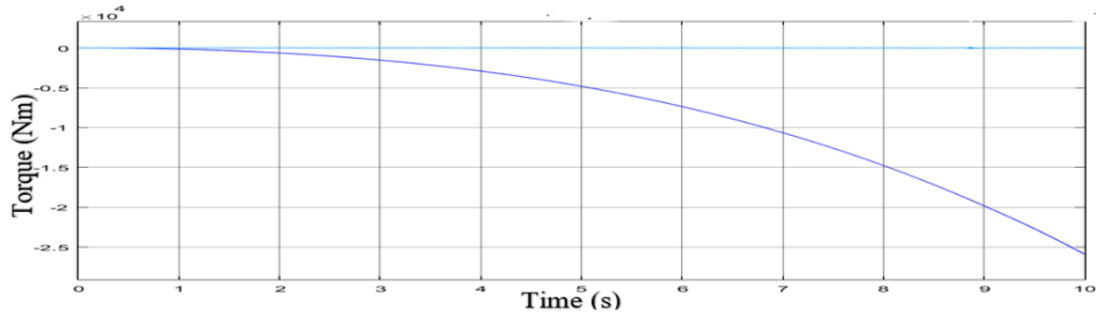


Fig 9. Variation of torque operating at the wind speed of 10 m/s against time.

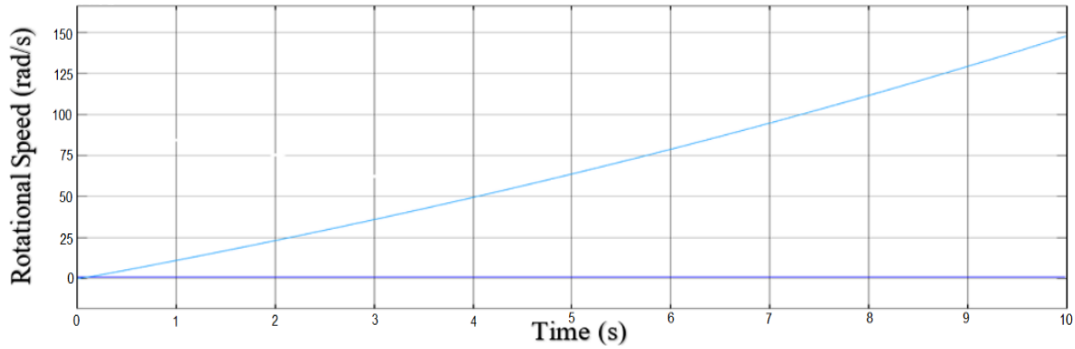


Fig 10. Variation of rotational speed of 10 m/s against time.

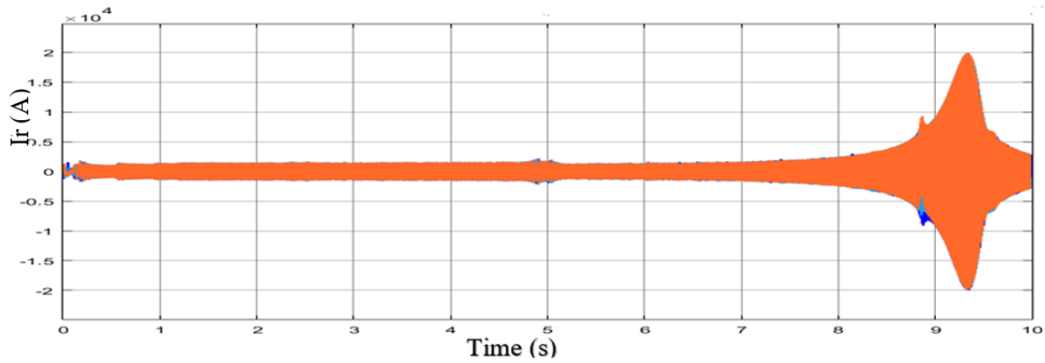


Fig 11. Graph of  $I_r$  against time when the WT generator is operating at super-synchronous mode at wind speeds of 10 m/s.

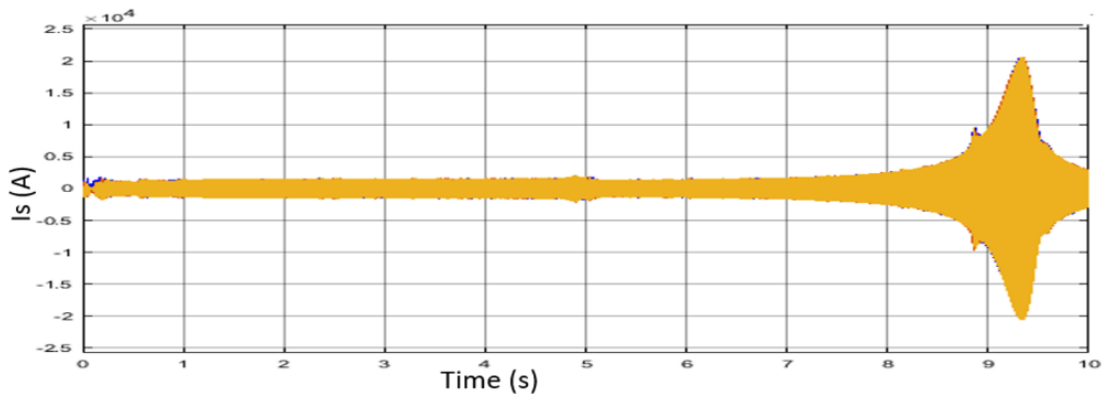


Fig 12. Variation of  $I_s$  against time when the WT generator is operating at super-synchronous mode at wind speed of 10m/s.

#### 4. STEADY-STATE PERFORMANCE OF THE WIND TURBINE GENERATOR BASED ON DFIG

It can be deduced that the electrical torque and mechanical power ( $T_{em}$  and  $P_t$ ) are input to the shaft of the Doubly-Fed Induction Machine (DFIM), making them equal regardless of the magnetizing strategy employed. The outcome for the DFIG torque, voltage, generated active power, and used reactive power are plotted for both magnetizing methods. While the influence of the two contrasted generation strategies does not cause significant differences in variables such as  $T_{em}$  and  $P_t$ , stator power ( $P_s$ ), and rotor power ( $P_r$ ), there are notable differences in the amplitudes of other variables such as stator current ( $I_s$ ), rotor current ( $I_r$ ), stator reactive power ( $Q_s$ ), and rotor reactive power ( $Q_r$ ) with respect to rotor speed.

The wind turbine application achieves the highest torques and powers at higher speeds (minimal slips). It is feasible to derive the steady-state behavior of the wind turbine generator at two different magnetizing levels, for example, with  $Q_s=0$  and with direct rotor current ( $I_{dr}=0$ ). It is noticed that magnetizing the machine via the stator ( $I_{dr}=0$ ) requires higher stator currents and lower rotor currents compared to magnetizing through the rotor ( $Q_s=0$ ). For this particular machine, efficiency is better when magnetizing through the stator. The active power of the stator significantly exceeds that of the rotor, achieving a peak value of around 2 MW. The active power of the rotor fluctuates between positive and negative values depending on the rotational speed. The steady-state simulation block diagram of the DFIG is as seen in Figure 13.

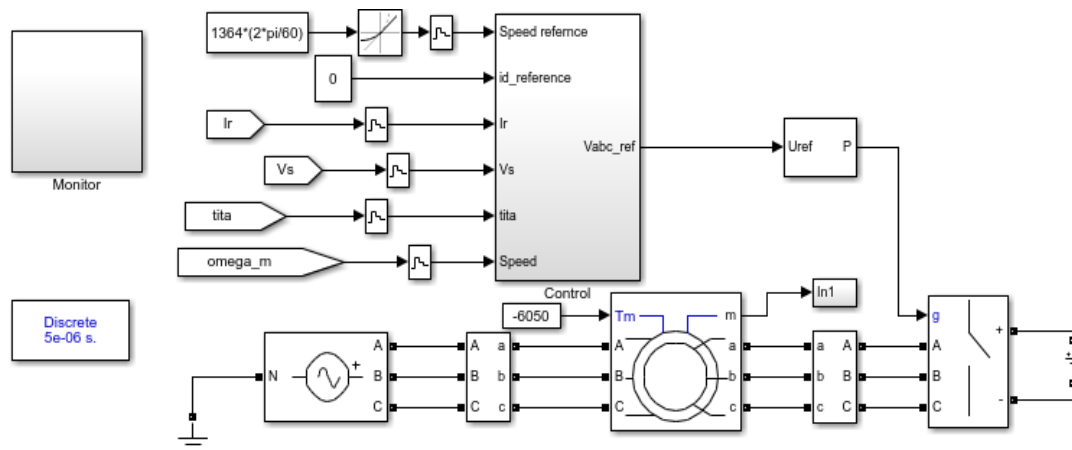


Fig 13. Steady-state simulation block diagram.

The  $I_d$  and speed references for the DFIG vector control were initially set to zero in the synchronous reference frame. The DFIG model produced three-phase measurement signals that were employed to ascertain  $I_r$  and  $V_s$ . The two inner control loops utilize transformation blocks to convert dq to DQ, DQ to abc, abc to DQ, and DQ back to dq. The Pulse width modulation (PWM) generator utilized a normalized triangular wave (-1 to 1). Therefore, the gain block with value of  $1/(V_{bus}/2)$  was utilized to normalized the control block output. A third harmonic injection was applied at the control output to obtain extra voltage for a specified DC-DC bus voltage. The stator voltage angle  $\theta$  and rotor angle  $\theta_m$ , were used to calculate the transformation angle  $\theta_r$ , which was then sent into the transformation blocks.

A speed PI regulator was implemented in the outer loop to ensure that the machine's speed remains within the specified upper and lower limits set by  $T_{em}$ . In the inner loop, two PI regulators were utilized to manage the  $I_d$  and  $I_q$  currents in accordance with their reference values. The transfer function of the designed system was employed to determine the  $K_p$  and  $K_i$  constant values. The transfer function of the



condition. The DFIG's generation model is designed to align with negative torque values, encompassing the range from negative slip to positive slip conditions.

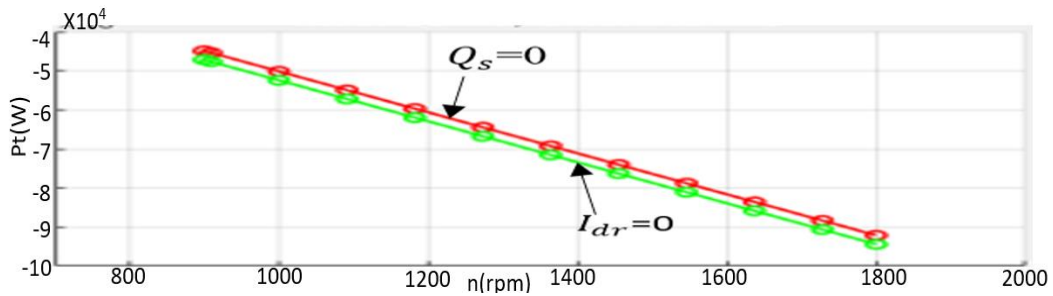


Fig 17. The active power against speed  $n$  (rpm). Green plot;  $I_{dr}=0$  and red plot;  $Q_s=0$ . This indicates the mechanical power at the shaft, determined by multiplying torque and speed.

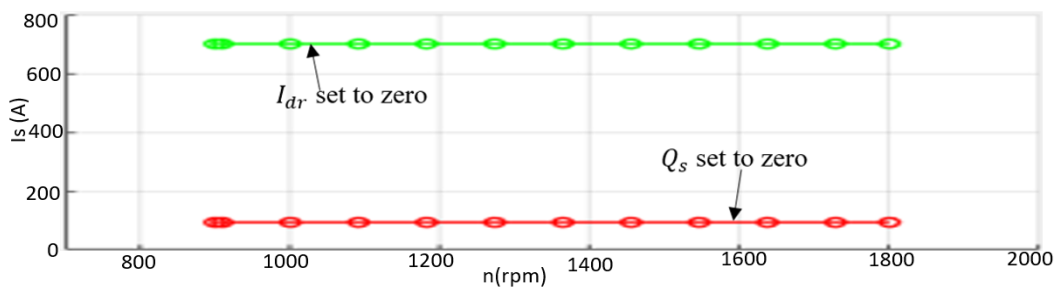


Fig 18. The stator current  $I_s$  (A) against speed  $n$ (rpm), green plot;  $I_{dr}=0$  and red plot  $Q_s=0$ .

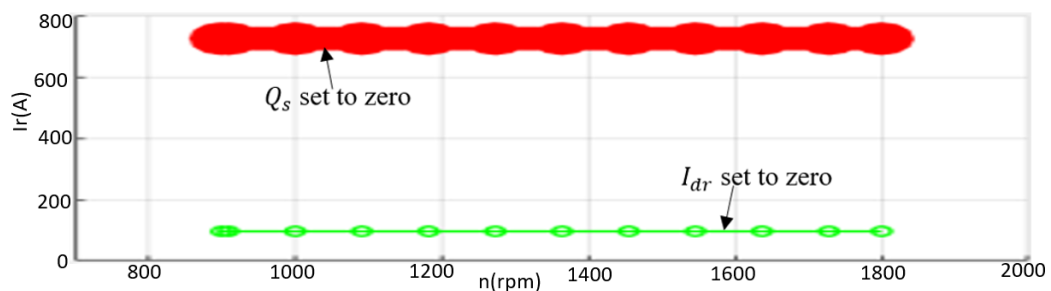


Fig 19.  $I_r$  (A) against speed  $n$  (rpm). Green plot;  $I_{dr}=0$ , red plot;  $Q_s=0$ . When  $Q_s$  is set to zero there is greater  $I_r$  than when  $I_{dr}$  is set to zero.

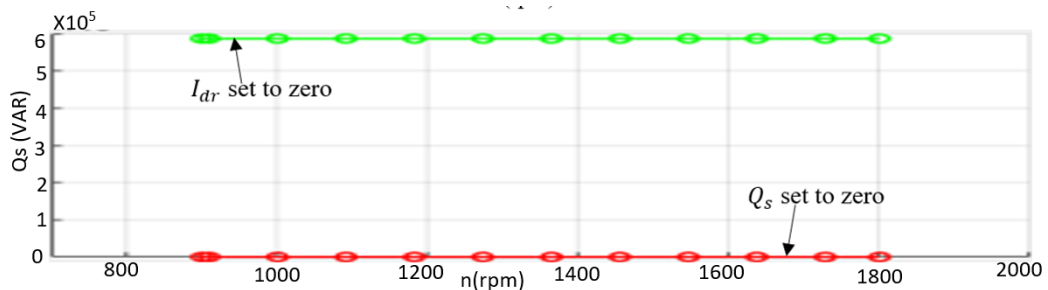


Fig 20.  $Q_s$  (VAR) against speed  $n$  (rpm), green plot;  $I_{dr}=0$ , red plot;  $Q_s=0$ . With  $I_{dr}$  set to zero more of  $Q_s$  is produced.

The reactive power of the rotor  $Q_r=0$  at synchronous mode of speed 1500 rpm, with either control method  $Q_s=0$  and  $I_{dr}=0$ , signifying the reactive power changes in accordance with the wind turbine speed (Fig. 21).

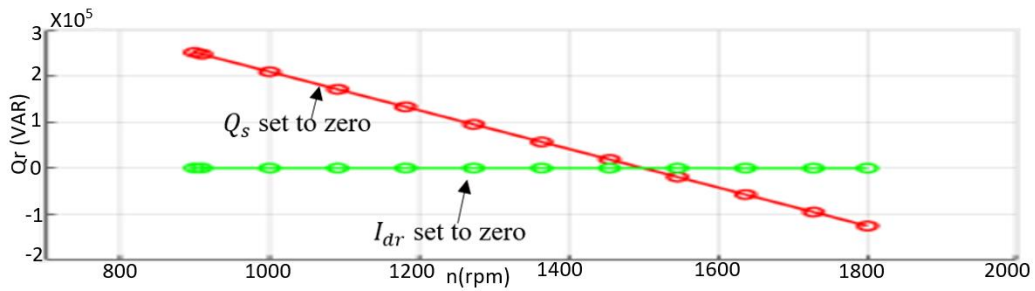


Fig 21.  $Q_r$  (VAR) against speed  $n$  (rpm), green plot;  $I_{dr}=0$ , red plot  $Q_s=0$ .

The stator is directly connected to the grid, which guarantees a consistent amplitude of voltage for the rotor. The magnitude of the rotor voltage changes in accordance with the speed of rotation. At synchronous mode, it is minimal. There are high voltages at both extremes. Here, the rotor operates relative to the stator, and these magnitudes represent relative values rather than actual magnitudes. If they are converted to the rotor side, the voltages will be very close to stator voltages.

The necessary amplitude of the rotor voltage is indicated, while the amplitude of the stator voltage stays constant due to its direct connection to the grid. Generally, it can be noted that an increase in slip within the module results in a higher required rotor voltage amplitude, which tends to zero as synchronism is achieved. At synchronous speed (1500 rpm), the stator is steady and low, with two peak voltage amplitudes at the minimum and maximum rotor speeds (Fig. 22).

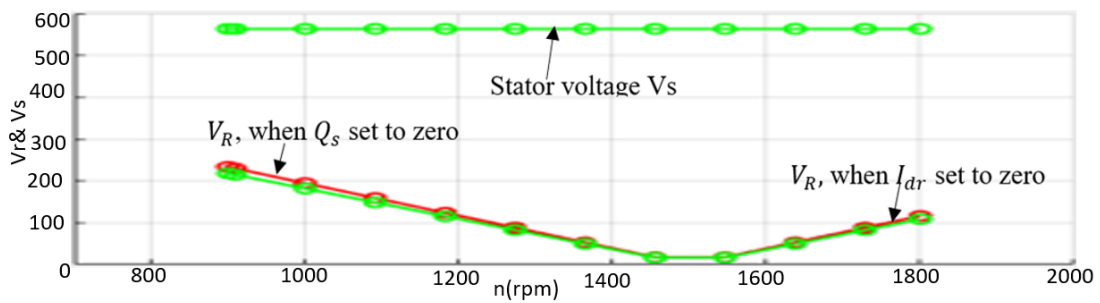


Fig 22.  $V_r$  and  $V_s$  against speed  $n$  (rpm), green plot :  $I_{dr}=0$ , red plot;  $Q_s=0$ .

There is maximum efficiency when the generator rotates at a synchronous speed of 1500 rpm.  $Q_r$  against speed in rpm is shown where  $Q_s$  is equal to zero and  $I_{dr}$  is equal to zero. With  $V_r$  set to zero at this same synchronous speed, its amplitude is too low (Fig. 23).

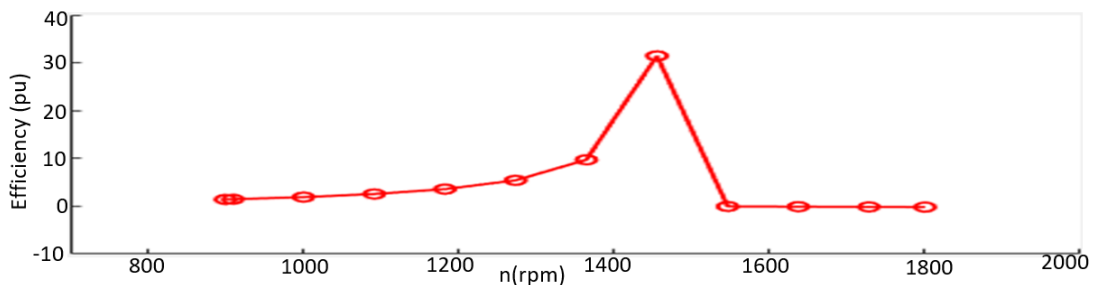


Fig 23. The efficiency of the DFIG at a Steady state.

## 5. CONCLUSION

This study aimed to explore the steady-state behavior of a Doubly Fed Induction Generator (DFIG) in relation to power system stability when integrated with a wind farm. Control of active and reactive

power from the rotor-side converter is accomplished by modulating the rotor current and the DFIG's speed. The DFIG's steady-state operation is sustained through two separate magnetization techniques: one applied to the stator and the other to the rotor. This occurs when the system operates in sub-synchronous mode and super-synchronous mode of wind speeds of 8m/s and 10m/s respectively, for these steady states, we have,  $I_{dr}=0$  and  $Q_s=0$ . The two magnetization methods are explained by developing an equivalent model of the DFIG in a dq reference frame based on mathematical equations.

The simulation results show that when the machine is magnetized through the stator, will result in constant reactive power and a higher stator current than when the machine is magnetized through the rotor. It is also noticed that higher efficiency is achieved when magnetized the DFIG through the stator rather than through the rotor.

The developed PI control unit assesses the grid-side converter by confirming that the generated power frequency and voltage align with those of the grid. An examination of the computed stator current, stator voltage, rotor current, and rotor position derived from encoder feedback signals reveals that the active PI control approach markedly improves the stability of the control system and bolsters its resistance to system noise. A notable advantage of this approach is its improved response to sudden load changes and significantly better torque performance at low speeds.

## REFERENCES

- Andersson, L. E., Anaya-Lara, O., Tande, J. O., Merz, K. O., & Imsland, L. (2021). Wind farm control - Part I: A review on control system concepts and structures. *IET Renewable Power Generation*, 15(10), 2085–2108. <https://doi.org/10.1049/rpg2.12160>
- Arnaltes, S., Rodriguez-Amenedo, J. L., & Montilla-D Jesus, M. E. (n.d.). *Control of variable*.
- Artigao, E., Martín-Martínez, S., Honrubia-Escribano, A., & Gómez-Lázaro, E. (2018). Wind turbine reliability: A comprehensive review towards effective condition monitoring development. *Applied Energy*, 228, 1569–1583. <https://doi.org/10.1016/j.apenergy.2018.07.037>
- Boukili, Y., Aguiar, A. P., & Carvalho, A. (2020). A DFIG-based Wind Turbine Operation under Balanced and Unbalanced Grid Voltage Conditions. *IFAC-PapersOnLine*, 53(2), 12835–12840. <https://doi.org/10.1016/j.ifacol.2020.12.1977>
- Chan, T. F., Lai, L. L., & Yan, L.-T. (2004). Performance of a Three-Phase AC Generator With Inset NdFeB Permanent-Magnet Rotor. *IEEE Transactions on Energy Conversion*, 19(1), 88–94. <https://doi.org/10.1109/TEC.2003.821861>
- Chen, Y., & Smedley, K. (2008). Three-Phase Boost-Type Grid-Connected Inverter. *IEEE Transactions on Power Electronics*, 23(5), 2301–2309. <https://doi.org/10.1109/TPEL.2008.2003025>
- Contreras Quispe, M. I., Caceres Cardenas, F. V., & Quispe, E. C. (2018). A Method for Steady State Analysis of Doubly Fed Induction Generator. *2018 IEEE ANDESCON*, 1–7. <https://doi.org/10.1109/ANDESCON.2018.8564721>
- Dahbi, A., Nait-Said, N., & Nait-Said, M.-S. (2016). A novel combined MPPT-pitch angle control for wide range variable speed wind turbine based on neural network. *International Journal of Hydrogen Energy*, 41(22), 9427–9442. <https://doi.org/10.1016/j.ijhydene.2016.03.105>
- Dao, C., Kazemtabrizi, B., & Crabtree, C. (2019). Wind turbine reliability data review and impacts on levelised cost of energy. *Wind Energy*, 22(12), 1848–1871. <https://doi.org/10.1002/we.2404>

- Eltamaly, A. M., Al-Saud, M., Sayed, K., & Abo-Khalil, A. G. (2020). Sensorless Active and Reactive Control for DFIG Wind Turbines Using Opposition-Based Learning Technique. *Sustainability*, 12(9), 3583. <https://doi.org/10.3390/su12093583>
- Fortmann, J. (2015). *Modeling of Wind Turbines with Doubly Fed Generator System*. Springer Fachmedien Wiesbaden. <https://doi.org/10.1007/978-3-658-06882-0>
- Gianto, R. (2021). Steady-state model of DFIG-based wind power plant for load flow analysis. *IET Renewable Power Generation*, 15(8), 1724–1735. <https://doi.org/10.1049/rpg2.12141>
- Hansen, A. D., & Michalke, G. (2008). Modelling and control of variable-speed multi-pole permanent magnet synchronous generator wind turbine. *Wind Energy*, 11(5), 537–554. <https://doi.org/10.1002/we.278>
- Haque, M. E., Negnevitsky, M., & Muttaqi, K. M. (2010). A Novel Control Strategy for a Variable-Speed Wind Turbine With a Permanent-Magnet Synchronous Generator. *IEEE Transactions on Industry Applications*, 46(1), 331–339. <https://doi.org/10.1109/TIA.2009.2036550>
- Heier, S. (2006). *Grid integration of wind energy conversion systems* (2nd ed). Wiley.
- Hua Geng, Geng Yang, Dewei Xu, & Bin Wu. (2011). Unified Power Control for PMSG-Based WECS Operating Under Different Grid Conditions. *IEEE Transactions on Energy Conversion*, 26(3), 822–830. <https://doi.org/10.1109/TEC.2011.2127478>
- I, N., Zhao, G., Yamin, Z., & Gul, w. (2020, November 19). Steady State performance Analysis of DFIG with Different Magnetizing Strategies in a Pitch-Regulated Variable Speed Wind Turbine. *Proceeding of the 2020 4th International Conference on Power and Energy Engineering (ICPEE)*.
- Kaloi, G. S., Wang, J., & Baloch, M. H. (2016). Active and reactive power control of the doubly fed induction generator based on wind energy conversion system. *Energy Reports*, 2, 194–200. <https://doi.org/10.1016/j.egyr.2016.08.001>
- Karakasis, N., Tsioumas, E., Jabbour, N., Bazzi, A. M., & Mademlis, C. (2019). Optimal Efficiency Control in a Wind System With Doubly Fed Induction Generator. *IEEE Transactions on Power Electronics*, 34(1), 356–368. <https://doi.org/10.1109/TPEL.2018.2823481>
- Karimirad, M. (2014). *Offshore energy structures for wind power, wave energy and hybrid marine platforms*. Springer.
- Keramat Siavash, N., Najafi, G., Tavakkoli Hashjin, T., Ghobadian, B., & Mahmoodi, E. (2020). Mathematical modeling of a horizontal axis shrouded wind turbine. *Renewable Energy*, 146, 856–866. <https://doi.org/10.1016/j.renene.2019.07.022>
- Li, S., & Li, L. (2021). Steady-state Solution and Evaluation Indices of DFIG Operating at Synchronous Speed (sDFIG). *2021 IEEE Sustainable Power and Energy Conference (iSPEC)*, 260–267. <https://doi.org/10.1109/iSPEC53008.2021.9736024>
- Mastoi, M. S., Tahir, M. J., Usman, M., Wang, D., Zhuang, S., & Hassan, M. (2022). Research on power system transient stability with wind generation integration under fault condition to achieve economic benefits. *IET Power Electronics*, 15(3), 263–274. <https://doi.org/10.1049/pel2.12228>
- Mousa, H. H. H., Youssef, A.-R., & Mohamed, E. E. M. (2021). State of the art perturb and observe MPPT algorithms based wind energy conversion systems: A technology review. *International Journal of Electrical Power & Energy Systems*, 126, 106598. <https://doi.org/10.1016/j.ijepes.2020.106598>
- Müller, S., Deicke, M., & Doncker, R. W. (2002). Doubly fed induction generator system for wind turbines. *IEEE Ind. Appl. Mag*, 8(3), 26-33,.

- Njiri, J. G., & Söffker, D. (2016). State-of-the-art in wind turbine control: Trends and challenges. *Renewable and Sustainable Energy Reviews*, 60, 377–393. <https://doi.org/10.1016/j.rser.2016.01.110>
- Nora, Z., Nadai, B., & Nadia. (2018, October 25). B.S.A. contribution to PI Control Speed of a Doubly Fed Induction Motor. *Proceeding of the 2018 6th International Conference on Control Engineering & International Technology (CEIT)*.
- Pande, J., Nasikkar, P., Kotecha, K., & Varadarajan, V. (2021). A Review of Maximum Power Point Tracking Algorithms for Wind Energy Conversion Systems. *Journal of Marine Science and Engineering*, 9(11), 1187. <https://doi.org/10.3390/jmse9111187>
- Robinson, J., Jovicic, D., & Joos, G. (2010). Analysis and Design of an Offshore Wind Farm Using a MV DC Grid. *IEEE Transactions on Power Delivery*, 25(4), 2164–2173. <https://doi.org/10.1109/TPWRD.2010.2053390>
- Sharawy, M., Shaltout, A. A., Abdel-Rahim, N., Youssef, O. E. M., & Al-Ahmar, M. A. (2021). Simplified Steady State Analysis of Stand-Alone Doubly Fed Induction Generator. *2021 22nd International Middle East Power Systems Conference (MEPCON)*, 246–251. <https://doi.org/10.1109/MEPCON50283.2021.9686219>
- Shourangiz-Haghighi, A., Haghnegahdar, M. A., Wang, L., Mussetta, M., Kolios, A., & Lander, M. (2020). State of the Art in the Optimisation of Wind Turbine Performance Using CFD. *Archives of Computational Methods in Engineering*, 27(2), 413–431. <https://doi.org/10.1007/s11831-019-09316-0>
- Tanvir, A., Merabet, A., & Beguenane, R. (2015). Real-Time Control of Active and Reactive Power for Doubly Fed Induction Generator (DFIG)-Based Wind Energy Conversion System. *Energies*, 8(9), 10389–10408. <https://doi.org/10.3390/en80910389>
- Xu, H., Nian, H., Xu, H., He, & Yikang. (2011). Dynamic modeling and improved control of DFIG under unbalanced and distorted grid voltage conditions. *Transactions On Energy Conversion*, 26, 1., <https://doi.org/10.1109/ISIE.2012.6237327>
- Zerzeri, M., Jallali, F., & Khedher, A. (2019). Robust FOC Analysis of a DFIM using an SMFO: Application to Electric Vehicles. *2019 International Conference on Signal, Control and Communication (SCC)*, 250–255. <https://doi.org/10.1109/SCC47175.2019.9116160>
- Zhou, Z., Mastoi, M. S., Wang, D., & Haris, M. (2023). Control strategy of DFIG and SVG cooperating to regulate grid voltage of wind power integration point. *Electric Power Systems Research*, 214, 108862. <https://doi.org/10.1016/j.epsr.2022.108862>